Spirals and vortex lattices in quasi-self-imaging divide-by-three optical parametric oscillators

M. Le Berre, E. Ressayre, and A. Tallet
Laboratoire de Photophysique Moléculaire du CNRS, Bâtiment 210, Université de Paris-Sud, 91405, Orsay Cedex, France
(Received 12 September 2005; published 29 March 2006)

A linear stability analysis is derived in self-imaging cavities for which the conditions for large Fresnel number are stated. In cases of both Fabry-Pérot and ring cavities a Hopf bifurcation is predicted at finite transverse wave number. The self-imaging Fabry-Pérot resonator operates as a longitudinal multimode cavity that invalidates the mean-field model. Above the bifurcation threshold, either vortex lattices, spirals, or targets occur, depending on the Fresnel number, the input intensity, and the mistunings. The time and spatial characteristics have different scales in the case of a self-imaging ring cavity, but the same sort of patterns are reported.

DOI: 10.1103/PhysRevE.73.036220 PACS number(s): 89.75.Kd, 42.65.Sf, 42.60.Da, 42.65.Yj

I. INTRODUCTION

The optical parametric oscillator (OPO) with plane mirror is an ideal laboratory for the study of spatial instabilities, when driven by a continuous plane-wave laser beam, in the limit of large Fresnel number. Theoretical works have, indeed, revealed many kinds of patterns, like periodic and quasiperiodic patterns, localized structures, vortices, and spirals [1–3], while experiments were generally performed with spherical cavities that preferentially give rise to patterns involving a few cavity eigenmodes [4–6].

Quasiconcentric cavities, which are self-imaging cavities, would be ideal cavities for the observation of any pattern, if the eigenmode waist did not vanish. Other self-imaging cavities were designed, which circumvent that difficulty. First, a ring cavity of full length close to $8f$, in which the crystal is symmetrically set between two pairs of confocal lenses with focal length f, was proposed for the theoretical study of transverse instabilities in a saturable medium [7]. Later Taranenko *et al.* [8] set up a self-imaging Fabry-Pérot resonator, of a full length close to $4f$, observing labyrinths and localized structures with a photorefractive medium. In the case of a ring cavity, they reported the formation of vortex lattices [9].

If a model was already developed in the case of the ring cavity [7], this paper is, to our knowledge, the first attempt at a theoretical approach for the quasi-self-imaging Fabry-Pérot resonator. We consider a nonlinear medium, in which the formation of spirals is expected, as discussed by several authors [10]. For that reason, we treat the case of an OPO where the signal and idler have different longitudinal wave numbers, more precisely a frequency divide-by-three (3:2:1) OPO [11], where spirals were displayed in the framework of the mean-field theory [12]. Here we start from the propagation model [3] which allows us to include the spherical cavity effects due to Fabry-Pérot geometry in the boundary conditions. Our analysis, devoted here to the OPO, can be very easily extended to other nonlinear systems.

The paper is organized as follows. We first show that a description in terms of transverse Fourier modes is well adapted to the study of instabilities. The linear stability analysis of the trivial state is given in detail in the case of the Fabry-Pérot resonator (Sec. II B) and briefly extended to the ring cavity (Sec. II C). In both cases, a Hopf bifurcation occurs, but with very different frequencies. Then the conditions for stable operation of the Fabry-Pérot cavity in the large Fresnel number limit are derived in Sec. III. In such cases, simulations display spirals and vortex lattices, when the Hopf bifurcation comes with a finite critical transverse wave number. The numerical time and space characteristics are found to agree with the linear stability analysis predictions. A homogeneous Hopf bifurcation can also occur in the ring cavity. In that case, only targets were obtained when varying the cavity mistunings.

II. LINEAR STABILITY ANALYSIS

A. Model equations

The amplitudes of the pump with angular frequency $3\omega_0$, the idler $(2\omega_0)$, and the signal (ω_0) are solutions of two sets of equations, the reduced Maxwell equations for the propagation inside the crystal plus the boundary conditions. Let α_j $(j=p,id,s)$ be the amplitudes for the pump, idler, and signal. The reduced Maxwell equations for the phase-matched beams are

$$\partial_z \alpha_p = i\nabla^2 \alpha_p/6n_p k_0 + i\alpha_s \alpha_{id}, \tag{1}$$

$$\partial_z \alpha_{id} = i\nabla^2 \alpha_{id}/4n_{id} k_0 + i\alpha_p \alpha_s^*, \tag{2}$$

$$\partial_z \alpha_s = i\nabla^2 \alpha_s/2n_s k_0 + i\alpha_p \alpha_{id}^*, \tag{3}$$

where ∇^2 is the transverse Laplacian, $k_0=\omega_0/c$ is the longitudinal wave number of the signal, and n_j $(j=p,id,s)$ is the refractive index.

The boundary conditions for a light beam with amplitude $E(z,\mathbf{r})$ and driving wave number k are determined with the help of the relation [13]

$$E(z_2,\mathbf{r}_0) = \frac{-ik}{2\pi C}\int d\mathbf{r}\, E(z_1,\mathbf{r}) \exp\frac{ik}{2C}(r^2 D - 2\mathbf{r}_0\cdot\mathbf{r} + A r_0^2) \tag{4}$$

which expresses the free-space propagation effects (including diffraction, lenses, etc.) from location z_1 to z_2 with the

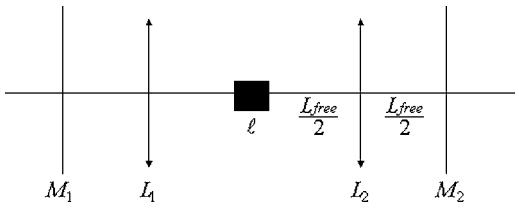

FIG. 1. Schema of the Fabry-Pérot resonator with mirrors $M_{1,2}$ and lenses $L_{1,2}$.

help of the matrix (A,B,C,D). They take different forms depending on whether the Fabry-Pérot (FP) or the ring cavity is in consideration.

B. Fabry-Pérot self-imaging symmetrical cavity

Let L be the distance between the two identical lenses and $L_{free}=L-\ell$, close to $2f$, where ℓ ($\ell \ll L$) is the crystal length. The distance between a lens and the nearest plane mirror is $L_{free}/2$, so that the free-space propagation length of the light between a crystal face and the nearest mirror is L_{free}.

For the light propagating from the ending face at $z=\ell$, going through the lens L_2, being reflected at mirror M_2, going again through L_2, and coming back to the ending face (Fig. 1), the matrix (A,B,C,D) is

$$\begin{pmatrix} -1+2g^2 & -2g/f \\ 2fg(1-g^2) & -1+2g^2 \end{pmatrix} \tag{5}$$

corresponding to a confocal cavity, with $g=1-L_{free}/2f$.

The Fourier mode basis is expected to be adapted to spherical self-imaging cavities, which approach plane-wave cavities. In a general manner, any transverse Fourier mode $e^{i\mathbf{K}\cdot\mathbf{r}}$ undergoes the transformation

$$\frac{1}{A}e^{ikr^2(A^2-1)/2AC-iK^2C/2kA}e^{i\mathbf{K}\cdot\mathbf{r}/A} \tag{6}$$

when using Eq. (4). Therefore for the half cavity trip described by matrix (5), any Fourier mode $e^{i\mathbf{K}\cdot\mathbf{r}}$ at $z=\ell$ comes back to the same location as

$$e^{i\mathbf{K}\cdot\mathbf{r}} \rightarrow -e^{-i\mathbf{K}\cdot\mathbf{r}} \tag{7}$$

in the limit $L_{free}\rightarrow 2f$. The relation (7) shows that the Fourier mode basis is well adapted to the study of self-imaging Fabry-Pérot resonators and allows one to simply express the boundary conditions. The change of the transverse wave vector $\mathbf{K}$ to $-\mathbf{K}$ and the phase lag π are consequences of confocality for the half cavity. For g not exactly zero, as in a real situation, the phase lag deviates from π by a small quantity $\Delta\varpi \approx K^2fg/k=K^2(2f-L_{free})/2k$. This phase shift depends on the driving beam wave number, which is in the ratio 3:2:1 for the pump, idler, and signal beams. The r-dependent phase shift in Eq. (6), also proportional to g, is neglected in this analysis. This r-dependent inhomogeneity can originate in the formation of targets instead of spirals, as shown by Hendrey *et al.* [14], when integrating an r-dependent complex Ginzburg-Landau equation.

Let the forward amplitudes be $F_{s,id}(t,\mathbf{r},z)$ and the backward amplitudes $B_{s,id}(t,\mathbf{r},z)$ for the signal and the idler, close to the lasing threshold. At $z=0$, the Fourier mode expansions $F_{s,id}=\Sigma e^{\lambda_K t}F_{s,id}(\mathbf{K},z)e^{i\mathbf{K}\cdot\mathbf{r}}$ and $B_{s,id}=\Sigma e^{\lambda_K t}B_{s,id}(\mathbf{K},z)e^{i\mathbf{K}\cdot\mathbf{r}}$ give rise to the boundary conditions, using Eq. (7),

$$\begin{pmatrix} F_s(\mathbf{K},0) \\ F_{id}^*(\mathbf{K},0) \end{pmatrix} = \mathbf{M}_{conf}\begin{pmatrix} B_s(-\mathbf{K},0) \\ B_{id}^*(-\mathbf{K},0) \end{pmatrix} \tag{8}$$

with

$$\mathbf{M}_{conf} = \begin{pmatrix} R_s e^{-i(\pi-\Delta\varpi_s-\theta_s)} & 0 \\ 0 & R_{id}e^{i(\pi+\Delta\varpi_{id}-\theta_{id})} \end{pmatrix} \tag{9}$$

where $R_{s,id}$ and $\theta_{s,id}$ are the mirror reflectivities and mistunings for signal and idler, respectively. These mistunings are those undergone in a full round trip of duration τ, because the phase mismatch between the forward and backward amplitudes is proportional to $2z$. Equivalently at $z=\ell$, the boundary conditions are

$$\begin{pmatrix} B_s(\mathbf{K},\ell) \\ B_{id}^*(\mathbf{K},\ell) \end{pmatrix} = \mathbf{M}_{conf}\begin{pmatrix} F_s(-\mathbf{K},\ell) \\ F_{id}^*(-\mathbf{K},\ell) \end{pmatrix}. \tag{10}$$

For the pump, the boundary conditions are

$$F_p(t,\mathbf{r},0) = E_0 + R_p e^{i\theta_p}B_p(t-\tau/2,\mathbf{r},0),$$

$$B_p(t,\mathbf{r},\ell) = R_p e^{i\theta_p}F_p(t-\tau/2,\mathbf{r},\ell), \tag{11}$$

where $B_p(t,\mathbf{r},0)$ and $F_p(t,\mathbf{r},\ell)$ are left hand members of Eq. (4). Assuming that the input pump beam is a plane wave and that the forward and backward pump beams are not modified in the crystal, i.e., $F_p(t,\ell)=F_p(t,0)$ and $B_p(t,0)=B_p(t,\ell)$, we get, at the lowest order, using Eq. (7) with $K=0$

$$F_p(t,0) = E_0 - R_p e^{i\theta_p}B_p(t-\tau/2,0),$$

$$B_p(t,0) = -R_p e^{i\theta_p}F_p(t-\tau/2,0). \tag{12}$$

Inside the crystal, solutions for the signal and idler forward amplitudes obey

$$\begin{pmatrix} F_s(\mathbf{K},\ell) \\ F_{id}^*(\mathbf{K},\ell) \end{pmatrix} = \mathbf{C}_F\begin{pmatrix} F_s(\mathbf{K},0) \\ F_{id}^*(\mathbf{K},0) \end{pmatrix} \tag{13}$$

with the nonlinear matrix, as deduced from Eqs. (2) and (3)

$$\mathbf{C}_F = \begin{pmatrix} e^{-i\ell K^2/2nk_0} & ie^{-i\ell K^2/2nk_0}F_p \\ -ie^{i\ell K^2/4nk_0}F_p^* & e^{i\ell K^2/4nk_0} \end{pmatrix} \tag{14}$$

where n is the refractive index in the crystal, assumed to be identical for the three beams. Solutions for backward amplitudes follow by replacing F_p by B_p in Eq. (13) and also in Eq. (14), giving rise to the matrix $\mathbf{C}_B$. Then applying $M_{conf}\mathbf{C}_B M_{conf}\mathbf{C}_F$ on $(F_s(\mathbf{K},\ell),F_{id}^*(\mathbf{K},\ell))^\dagger$ and using Eqs. (8)–(14), we get the characteristic equation

$$e^{2\lambda\tau} - 2e^{\lambda\tau+i\Omega}R^2(\cos\Phi - R_p|F_p|^2) + R^4 \times e^{2i\Omega}[1 + R_p^2|F_p|^4 - (1+R_p^2)|F_p|^2] = 0 \quad (15)$$

with $\Omega = \theta_s - \theta_{id} - \tilde{\ell}K^2/4k_0$, $\Phi = \theta_s + \theta_{id} - 3\tilde{\ell}K^2/4k_0$, and $F_p = E_0/(1-R_p^2 e^{i\theta_p})$, where $\tilde{\ell} = \ell/n + L_{free} - 2f$ is the effective diffraction length for a half round trip. $R_{id} = R_p = R$ is also assumed. At threshold [$\mathrm{Re}(\lambda = \alpha + i\beta) = 0$], Eq. (15) exhibits a Hopf bifurcation with

$$\beta\tau = \Omega + \pi = \pi + (\theta_s - \theta_{id} - \tilde{\ell}K^2/4k_0) \quad (16)$$

at finite transverse wave number K_{crit},

$$\frac{3\tilde{\ell}}{4k_0}K_{crit}^2 = (\pi + \theta_s + \theta_{id}) \quad (\Phi = \pi) \quad (17)$$

(here $\tilde{\ell}$ is assumed to be positive). The threshold input is easily deduced from Eqs. (15)–(17)

$$E_0^{th} \simeq \frac{(1-R^2)|1 - R^2 e^{i\theta_p}|}{2R\sqrt{R}} \quad (18)$$

with $R_p \approx R \approx 1$. Assuming $\theta_{s,id} \ll 1$, Eqs. (16) and (17) give rise to

$$\beta\tau \approx 2\pi/3, \quad (19)$$

i.e., a period equal to $T = 3\tau$. Let us note that mod(2π) solutions for K_{crit} are irrelevant because the period $2\pi/\beta$ cannot be smaller than the round-trip time.

In the same conditions, a divide-by-2 OPO would display a homogeneous Hopf bifurcation with period 2τ.

C. Ring self-imaging symmetrical cavity

Any Fourier mode is assumed to be recovered at $z = 0$ after a full round trip, as displayed by using Eq. (7) twice, with a phase $2K^2 fg/k$. Let $\tilde{\tilde{\ell}} = \ell/n + 2L_{free} - 4f$ be the effective diffraction length. For $\tilde{\tilde{\ell}}(\theta_s + \theta_{id}) > 0$, there is a Hopf bifurcation with finite critical wave number characterized by

$$\beta\tau = (2\theta_s - 4\theta_{id})/3,$$

$$K_{crit}^2 = 4k_0/3\tilde{\tilde{\ell}}(\theta_s + \theta_{id}), \quad (20)$$

and $F_p^{th} = (1-R^2)/R^2$ if we assume two mirrors with reflectivity R. For $\tilde{\tilde{\ell}}(\theta_s + \theta_{id}) \leqslant 0$, we recover a homogeneous Hopf bifurcation with $\beta\tau = (\theta_s - \theta_{id})/2$ as predicted with the mean-field model [12].

III. NUMERICAL RESULTS

Simulations have been performed for the FP and ring cavities, using data close to an experimental situation. For the crystal, we take typical values given to us by Zondy, in case of phase matching, $\Delta k = 3n_p - 2n_{id} - n_s = 0$, with slightly different refractive indices (2.17, 2.15, and 2.10). The propagation inside the crystal of length $\ell = 0.25$ cm is treated by a split and step method, integrating the coupled reduced Maxwell equations for the three beams with step $\Delta z = 0.1\ell$. The light propagation from an ending face of the crystal, going through the lens with $f = 2.5$ cm and arriving at the mirror with $R = 0.95$, is calculated with the help of the integral (4). Numerical results were checked using different grid lengths and numbers (512×512 or 1024×1024). Finally, a flat circular input amplitude $E_0 e^{-(r/4w_p)^{16}}$ is chosen (variations of the input waist input only change the threshold input). The waist for any beam is determined from the associated Rayleigh length, as usual for spherical cavities [15]. Close to the self-imaging condition, the Rayleigh length for the FP cavity is $z_d = f\sqrt{-\tilde{\ell}/2fg}$. Figure 2 shows that this resonator is unstable for $2f - \ell/n < L_{free} < 2f$. Furthermore the Rayleigh length diverges for $L_{free} - 2f \to 0$ by positive values, giving rise to infinite waists.

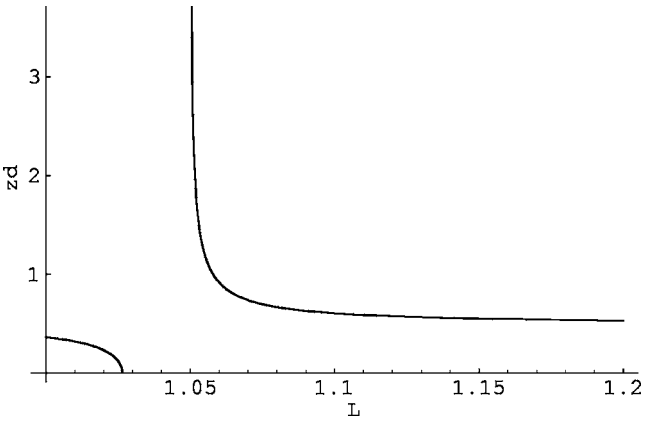

FIG. 2. Rayleigh length scaled to $2f$ as a function of $L/2f$ for the Fabry-Pérot cavity.

Lasing occurs above the Hopf bifurcation threshold as predicted by the linear stability analysis.

In case of the Fabry-Pérot resonator, the time trace of the complex amplitudes displays the 3τ period, as predicted in Eq. (19) for small mistunings. The motion is generally quasiperiodic, the slow period being close to $2\pi/(\theta_s - \theta_{id})$, which is the first Hopf bifurcation period for a filled-up resonator without lenses. This slow period probably appears here as a second Hopf bifurcation, associated with $K^2 \simeq 0$. The threshold input $E_0^{th} \simeq 0.07$ is much larger than the prediction given by Eq. (18). This discrepancy is not surprising because Eq. (18) has been obtained for a plane-wave input. Either lattices of vortices, spirals, or targets appear for different L, θ_s ($\theta_{id} = 0$ in any case), and E_0. They were never found to coexist in the investigated domains of parameters. For instance, with $L = 5.3$ cm, $\theta_s = 0.2$, and Fresnel number $N = z_d/\tilde{\ell} \simeq 26$, a vortex lattice occurs, as displayed in Fig. 3 by the real part of the amplitude (b) and the stationary intensity (a). The numerical wave number of this lattice is about $6.7w_p^{-1}$ and agrees qualitatively with the critical value deduced from Eq. (17), equal here to $8.7w_p^{-1}$. This structure is stable; it occurs for larger mistunings and a large range of the input E_0.

Figure 4 reports patterns for $L = 5.5$ cm ($N \simeq 8$) and $\theta_s = 0.3$: A spiraling pattern occurs close to the threshold [Fig.

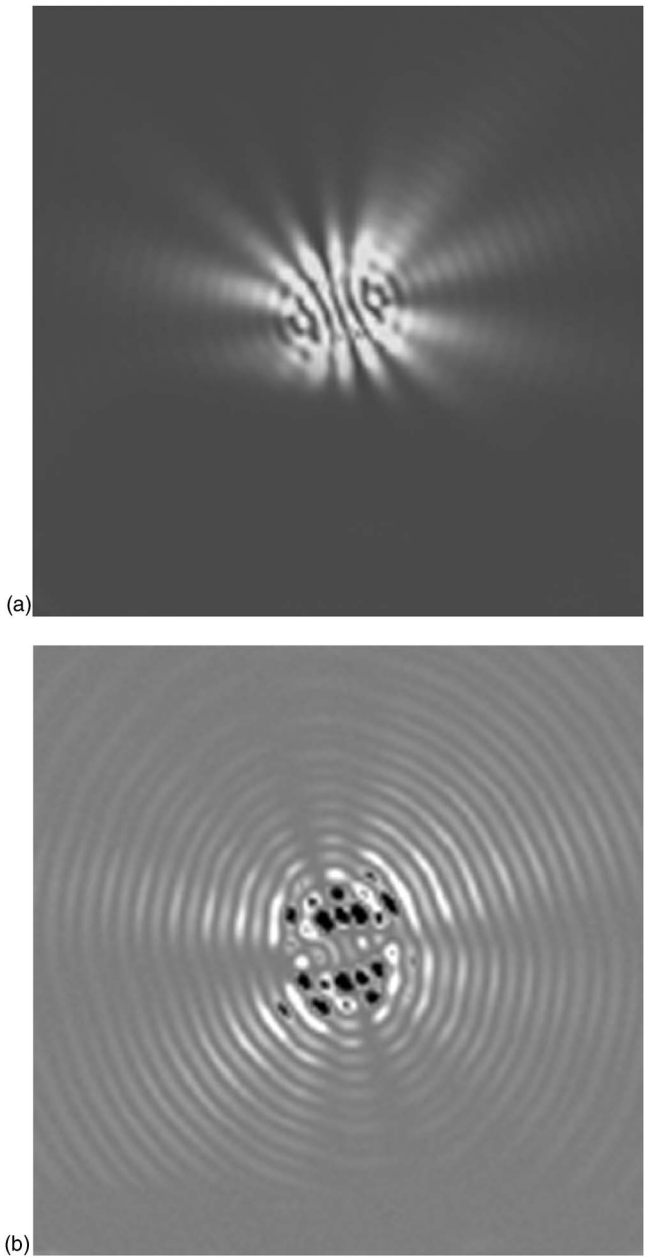

FIG. 3. Fabry-Pérot resonator with $L_{free}=5.05$ cm. Intensity (a) and real part (b) of the signal amplitude. The full window is $15w_p$.

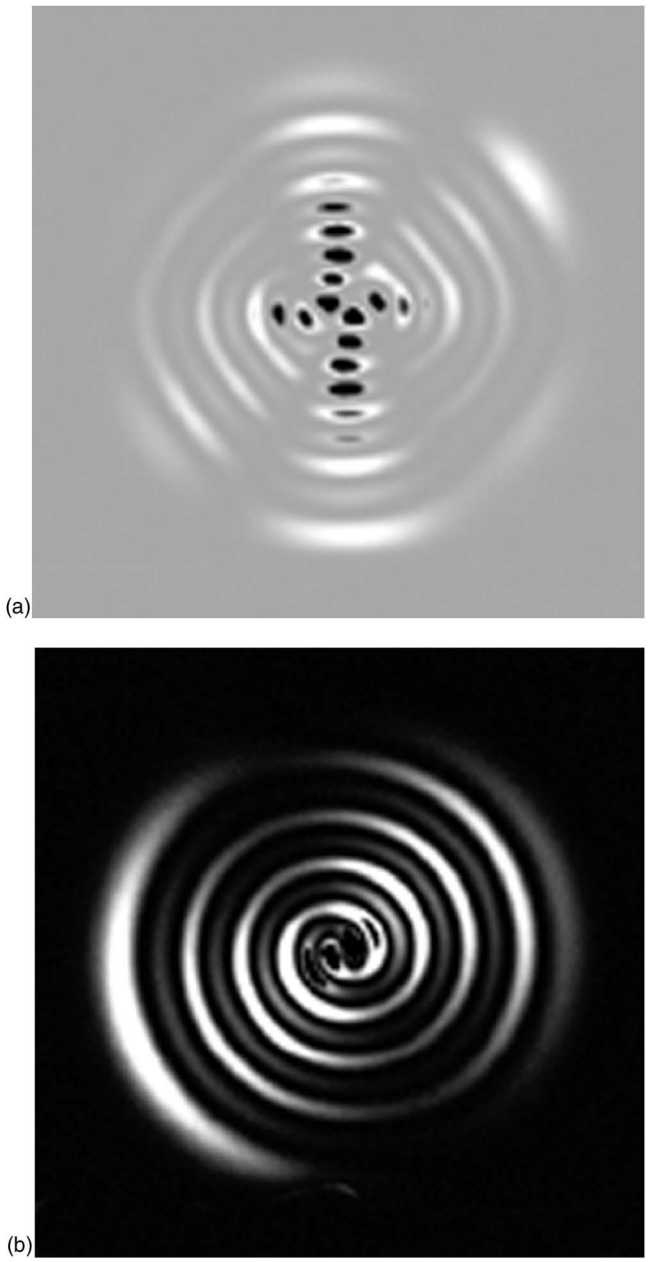

FIG. 4. Fabry-Pérot resonator with $L_{free}=5.25$ cm. Real part of the signal amplitude for $E_0=0.07$ (b) and 0.12 (a). Same window as in Fig. 3.

4(b)], which makes a 2π revolution in a time equal to the slow period $2\pi/\theta_s$; the intensity pattern displays eight concentric rings. Far above the threshold, the spiral destabilizes, giving rise to a nonstationary vortex lattice, as shown on Fig. 4(a).

At $L=5.6$ cm, a target occurs for $\theta_s=0.1$ with six rings as shown in Fig. 5, while a spiral is formed for $\theta_s=0.5$, with seven rings on the intensity profile.

These results show that the patterns are very sensitive to θ_s. They show also that vortex lattices can occur for finite Fresnel number, far enough from the unstable regime where z_d diverges (see Fig. 2).

For the ring cavity, the same patterns are expected, while with a different space scaling because of smaller critical wave number, and with a slow time period. [Compare Eqs. (17) and (19) with Eq. (20)]. Vortices occur on the trivial unstable state for $L=5.3$ cm, $\theta_s=0.5$, and $E_0=0.07$, as shown in Fig. 6(a). For a higher input, $E_0=0.14$ and $\theta_s=0.3$, the nontrivial homogeneous state destabilizes, giving rise to a spiraling pattern, as shown in Fig. 6(b). Spirals have also been obtained on the trivial unstable state.

IV. DISCUSSION

The above linear analysis has taken lensing and propagation effects outside the crystal into account phenomenologically, introducing only dephasing terms. The Fourier mode expansion is an approximation that allowed us to pre-

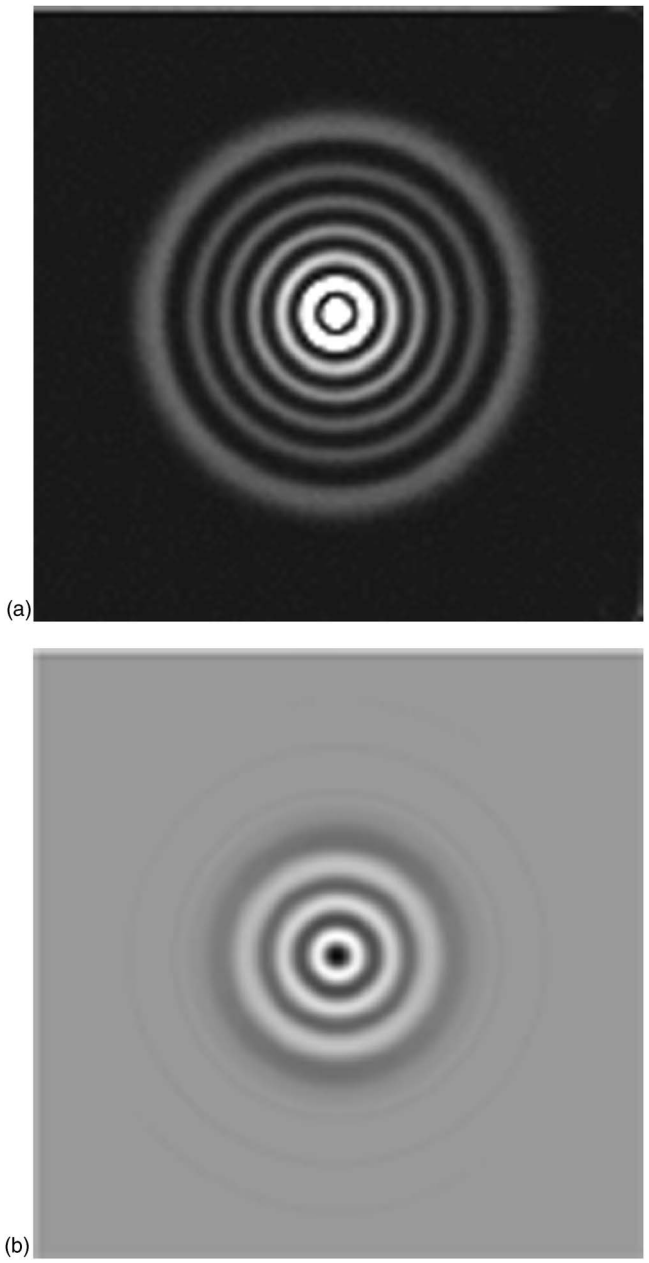

FIG. 5. Fabry-Pérot resonator with $L_{free}=5.35$ cm, $E_0=0.12$, $\theta=0.1$. (a) Stationary intensity. (b) Real part of the signal amplitude at a given time. Same window as in Fig. 3.

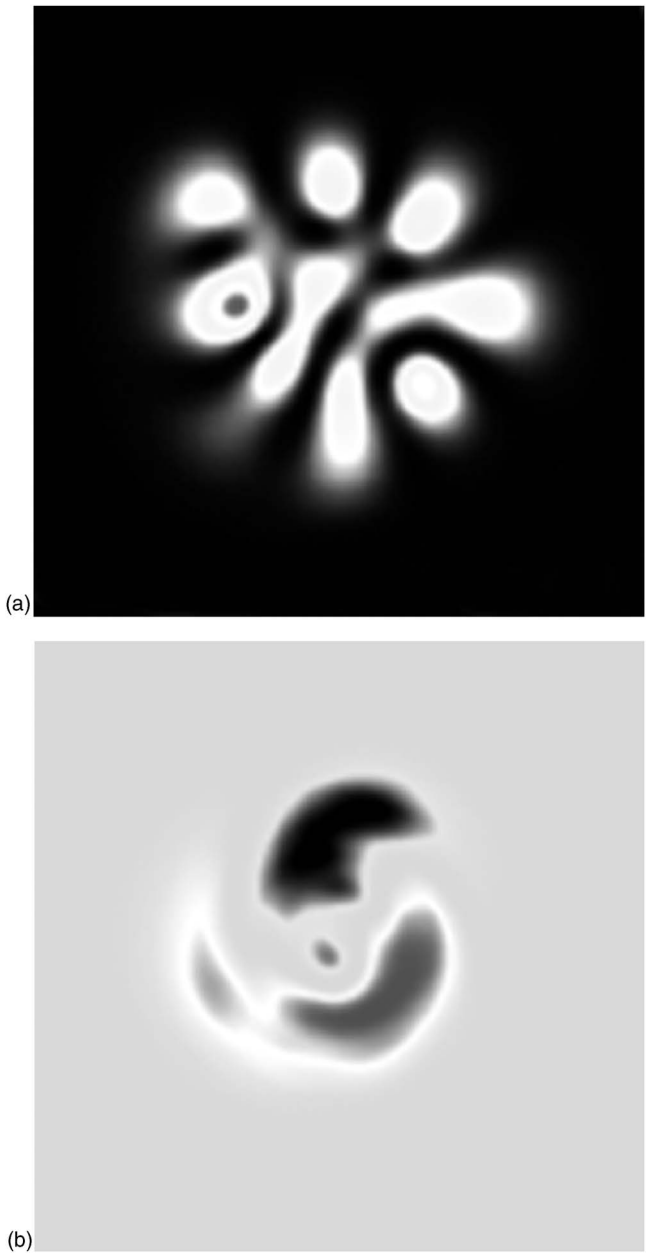

FIG. 6. Ring cavity. Signal intensity for $L_{free}=5.05$ cm (a) and real part of the amplitude for $L_{free}=5.3$ cm (b). The full window is $7.5w_p$.

dict the Hopf bifurcation period and the critical wave number for both the Fabry-Pérot resonator [Eqs. (16) and (17)] and the ring cavity [Eq. (20)]. This analysis has pointed out the scale differences for the transverse space and time variables between a Fabry-Pérot and a ring cavity. For the Fabry-Pérot resonator, the period is equal to 3τ (2τ) for a divide-by-three (two) OPO. This result implies a longitudinal multimode operation [3] that invalidates the mean-field model. For a self-imaging ring cavity, the characteristic time is much larger than the round-trip time, so that the mean-field model applies.

The patterns in Figs. 3–5 occur for very small effective diffraction lengths, i.e., for large but *finite* Fresnel numbers. They look like the patterns observed in photorefractive medium experiments [9]. In our simulations, vortex lattices occur for $L=5.3$ cm, as well as for $L=5.5$ cm, i.e., when the Fresnel number has decreased by a factor about 3. Nevertheless the single spiral is found only for "small" Fresnel number, as in the latter experiment.

These spirals are fully nonlinear patterns, differently from the structures occurring in a confocal resonator, which are superpositions of a few cavity eigenmodes [6]. We have not derived a nonlinear analysis close to the Hopf threshold but we may infer that, in the ring cavity case, the amplitude equations would be of complex Swift-Hohenberg or Ginzburg-Landau types, depending on the sign of $\tilde{\tilde{\ell}}(\theta_s+\theta_{id})$. These equations were derived in the case of a plane mirror ring cavity [10]. In our case

the lensing effect term $e^{ikgr^2/f}$ should be taken into account, introducing in the amplitude equation a small r-dependent term due to spherical mirrors. As an example, the ring cavity vortex lattices shown in Fig. 6(a) for positive $\tilde{\tilde{\ell}}(\theta_s + \theta_{id}) > 0$ are interpreted as solutions of a complex Swift-Hohenberg equation. For the opposite inequality, solutions of the complex Ginzburg-Landau are expected. In that case, our simulations have displayed no spirals but only targets.

In conclusion, quasi-self-imaging cavities are very promising for the observation of transverse instabilities analyzed in the framework of plane mirror cavities.

ACKNOWLEDGMENTS

Jean-Jacques Zondy is gratefully acknowledged for stimulating discussions. The numerical simulations were realized at the Institut du Développement et des Ressources Informatiques du Centre National de la Recherche Scientifique and their results were treated at the Centre de Ressources Informatiques of the Paris-Sud Université.

[1] For a review, see Paul Mandel and M. Tlidi, J. Opt. B: Quantum Semiclassical Opt. **6**, R60 (2004), and references herein.
[2] For a review, see K. Staliunas and V. J. Sanchez-Morillo, Springer Tracts in Modern Physics, Vol. 183 (Springer, Berlin, 2003), and references herein.
[3] M. Le Berre, D. Leduc, S. Patrascu, E. Ressayre, and A. Tallet, Chaos, Solitons Fractals **10**, 627 (1999).
[4] M. Vaupel, A. Maître, and Claude Fabre, Phys. Rev. Lett. **83**, 5278 (1999); S. Ducci, N. Treps, A. Maître, and C. Fabre, Phys. Rev. A **64**, 023803 (2001).
[5] P. Suret, D. Derozier, M. Lefranc, J. Zemmouri, and S. Bielawski, J. Opt. Soc. Am. B **19**, 395 (2002).
[6] M. Le Berre, E. Ressayre, and A. Tallet, Phys. Rev. E **67**, 066207 (2003).
[7] S. Patrascu, C. Nath, M. Le Berre, E. Ressayre, and A. Tallet, Opt. Commun. **91**, 433 (1992).
[8] V. B. Taranenko, K. Staliunas, and C. O. Weiss, Phys. Rev. Lett. **81**, 2236 (1998).
[9] C. O. Weiss, M. Vaupel, K. Staliunas, G. Slekys, and V. B. Taranenko, Appl. Phys. B: Lasers Opt. **68**, 151 (1999).
[10] S. Longhi, Phys. Rev. A **53**, 4488 (1996); V. J. Sanchez-Morcilo, E. Roldan, G. J. de Valcarcel, and K. Staliunas, *ibid.* **56**, 3237 (1997); Z. H. Muslimani, Physica A **249**, 141 (1998).
[11] A. Douillet, J. J. Zondy, A. Yelisseyev, S. Lobanov, and L. Isaenko, J. Opt. Soc. Am. B **16**, 1481 (1999).
[12] S. Longhi, Phys. Rev. E **63**, 055202(R) (2001).
[13] S. A. Collins, J. Opt. Soc. Am. **60**, 1168 (1970).
[14] M. Hendrey, K. Nam, P. Guzdar, and E. Ott, Phys. Rev. E **62**, 7627 (2000).
[15] A. E. Siegman, *Lasers* (University Science, Mill Valley, CA, 1986).